A thermally self-sustained micro-power plant with integrated micro-solid oxide fuel cells, micro-reformer and functional micro-fluidic carrier

Author preprint, accepted manuscript

Original version: Journal of Power Sources, 2014

http://hdl.handle.net/10.1016/j.jpowsour.2014.02.039

Barbara Scherrer[*1,2,3], Anna Evans[1], Alejandro J. Santis-Alvarez[4], Bo Jiang[5,6], Julia Martynczuk[1,7], Henning Galinski[1,2,8], Majid Nabavi[4], Michel Prestat[1], René Tölke[1], Anja Bieberle-Hütter[1,9], Dimos Poulikakos[4], Paul Muralt[5], Philippe Niedermann[10], Alex Dommann[10], Thomas Maeder[6], Peter Heeb[11], Valentin Straessle[11], Claude Muller[10] and Ludwig J. Gauckler[1]

[1] Nonmetallic Inorganic Materials, ETH Zurich, Zurich, Switzerland

[2] Nanometallurgy, ETH Zurich, Zurich, Switzerland

[3] Australian Center of Microscopy and Microanalysis, University of Sydney, Sydney, Australia

[4] Laboratory of Thermodynamics in Emerging Technologies, ETH Zurich, Zurich, Switzerland

[5] Ceramics Laboratory, EPFL, Lausanne, Switzerland

[6] Laboratory of Microengineering for Manufacturing, EPFL, Lausanne, Switzerland

[7] Electron Microscopy ETH Zurich (EMEZ), ETH Zurich, Zurich, Switzerland

[8] School of Engineering and Applied Sciences, Harvard University, Cambridge, United States of America

[9] current affiliation: FOM Institute DIFFER (Dutch Institute for Fundamental Energy Research), Nieuwegein, Netherland.

[10] entre Suisse d'Electronique et Microtechnique, CSEM, Neuchâtel, Switzerland

[11] Institute for Micro- and Nanotechnology, NTB, Buchs, Switzerland

[*]corresponding author: barbara.scherrer@mat.ethz.ch, Nanometallurgy, ETH Zurich, HCI G527, Vladimir-Prelog-Weg 5, 8093 Zurich, Switzerland, Phone: +41 44 632 2592, Fax: +41 44 632 1101

Keywords: micro-power plant, micro-solid oxide fuel cell, thin films, butane reformation, chemical micro-reactors, catalytic partial oxidation, thermally independent

Abstract

Low temperature micro-solid oxide fuel cell (micro-SOFC) systems are an attractive alternative power source for small-size portable electronic devices due to their high energy efficiency and density. Here, we report on a thermally self-sustainable reformer – micro-SOFC assembly. The device consists of a micro-reformer bonded to a silicon chip containing 30 micro-SOFC membranes and a functional glass carrier with gas channels and screen-printed heaters for start-up. Thermal independence of the device from the externally powered heater is achieved by exothermic reforming reactions above 470 °C. The reforming reaction and the fuel gas flow rate of the n-butane/air gas mixture controls the operation temperature and gas composition on the micro-SOFC membrane. In the temperature range between 505 °C and 570 °C, the gas composition after the micro-reformer consists of 12 vol.% to 28 vol.% H_2. An open-circuit voltage of 1.0 V and maximum power density of 47 mW cm^{-2} at 565 °C is achieved with the on-chip produced hydrogen at the micro-SOFC membranes.

Introduction

Miniaturized fuel cell systems are an attractive alternative power source for small size electronic devices with a power range of 1-20 W. For polymer electrolyte membrane fuel cells (PEMFC) such products are already commercialized by Horizon [1] and Intelligent Energy Limited [2] and for direct methanol fuel cells (DMFC) products are announced by MTI Micro [3]. PEMFCs require pure hydrogen as a fuel gas which involves expensive external fuel reforming and storage. The drawbacks of DMFCs are the need for concentrated toxic methanol to achieve appreciable energy densities. Micro-solid oxide fuel cells (micro-SOFCs) operate at higher temperatures, and therefore, high-energy density and high specific energy hydrocarbon fuels such as propane or butane can be used. ONEBAT™ is such a micro-SOFC

system consisting of electrochemically-active micro-SOFC membranes fabricated on a micro machined chip, a gas processing unit composed of a fuel reformer, an exhaust gas post-combustor and a thermal management system and insulation [4-6]. Nectar™, a similar system based on micro-SOFC membranes is announced for commercialization, however, so far the product is not available [7]. A few patents about possible designs of an micro-power plant based on micro-SOFC membranes are available [8, 9].

Planar free-standing micro-SOFC membranes consisting of an YSZ electrolyte and Pt electrodes have been mostly tested [10-16]. Their power densities were measured in an external furnace or on a hot plate with pure hydrogen or hydrogen diluted with inert gases as fuel. A few publications report about anodes based on Pt, Pd or Ru, which were tested in fuels consisting of methane or a methane-air mixture reformed *in situ* on the anodes [17-21]. Butane, one of the main constituents of liquid petroleum gas (LPG), has several advantages over methane and hydrogen based fuels. At 4 bar pressure, butane is liquid at room temperature which enables easy storage and results in a higher energy density than methane. Additionally, butane is thermodynamically less stable than methane and is thus easier to reform. Takagi *et al.* [22] recently published tests of micro-SOFC membranes under natural gas (main constituents: methane) as fuel. They achieved a power density of 800 mW cm^{-2} at 530 °C with *in situ* reformation at the Ru anode of humidified natural gas. An *in situ* reforming means that the partial oxidation of the fuel happens at the anode which is thermodynamically more efficient than *ex situ* reformation. The direct reformation uses catalytic sites of the anode, which therefore cannot be used for the hydrogen oxidation [18] reducing the power density of the micro-SOFC. A separation of the fuel reforming and the micro-SOFC allows optimizing the reformation and should lead to a higher power density [23-25]. As the full oxidation of the fuel to CO_2 and H_2O leads to hot spots at the locations where the exothermic reforming reaction takes place, the resulting inhomogeneous

temperature distribution at the micro-SOFC membranes lead to degradation of the anode microstructure [23]. The separation of the reforming reaction of the fuel from the micro-SOFC might overcome this drawback. Furthermore, a spatial separation of the reformer and the anode reactions potentially makes the system more flexible for the use of different fuels and the catalyst in the reformer can be adjusted accordingly independent from the anode material and thus carbon poisoning of the anode can be minimized [23]. For the partial oxidation of light hydrocarbons, Ni, Ir, Pt, Pd and Rh on different support materials were tested as reformation catalysts [26, 27]. Platinum, the most commonly used electrode material in micro-SOFC membranes, has a high tendency for dehydration and thereby forms hydroxyls which lead to carbon deposition at the Pt. Overall, Rh was identified to have the best conversion rate and the highest selectivity for H_2 production among the tested catalyst materials [26]. The use of a Rh catalyst in the reformer enables Pt electrodes and still avoids cracking products at the electrode.

In this work, the results of a thermally self-sustained reformer combined micro-fuel cell assembly of the ONEBAT™ system are reported. The device was fueled with n-butane in air. With an integrated heater, the device was started until the self-sustained partial oxidation reaction of the n-butane in the micro-reformer kicks in. As reformer catalyst, 1.9 wt.% Rh on $Zr_{0.5}Ce_{0.5}O_2$ was used. An array of 30 individual free-standing micro-SOFC membranes consisting of a Pt-3YSZ-Pt multilayer was fabricated on a silicon chip. The performances of the micro-reformer as well as the electrochemical properties of individual micro-SOFC membranes are reported. To the authors' knowledge this is the first demonstration of such integrated micro power plant based on micro-SOFC technology.

Experimental

Fabrication

Functional carrier

A functional carrier (Figure 1) was designed for gas feeding and start-up energy. It is fabricated using thick-film techniques described in detail elsewhere [28]. The functional carrier consisted of two borosilicate glass wafers (Schott AF32, Schott AG) with dimensions of 14 mm × 75 mm × 0.7 mm. The Pt heaters (CL11-6109, Heraeus) were screen-printed at the bottom of the carrier and the glass walls were fabricated between two glass layers using glass frit (Ferro IP 760c, Ferro Corporation). Hermetic sealing was achieved after firing in air at 700 °C for 20 min. This results in a cross-section of about 0.15 mm × 5.3 mm of the fluidic channels. At the "cold"-end of the carrier, a ceramic plate connected the heater to the start-up power supply.

Micro-reformer

The planar structure of the micro-reformer (Figure 1) allows a compact assembly design. The micro-reformer was fabricated by anodic bonding of a 1000 µm thick Borofloat 33 glass to an etched 1000 µm thick Si-substrate. The reactor cavity had a depth of 0.65 mm and a total volume of 134.8 mm^3.

The 1.9 wt.% Rh on $Ce_{0.5}Zr_{0.5}O_2$ catalytic nanoparticles with an average diameter of 12 nm were synthesized in a one-step process by flame spray synthesis [29]. The reactor cavity was filled with a catalytic ceramic foam prepared by a one-step sol-gel process as described elsewhere [30]. In short, 15 wt.% catalytic nanoparticles, 80 wt.% washed and calcined SiO_2-sand (Riedel-deHaën, average diameter: 200 µm, puriss p.a.), 2 wt.% gelation agent (triammonium citrate, Riedel-deHaën, purity ≥ 97%) and 3 wt.% ceramic binder (sodium

metasilicate pentahydrate, Riedel-deHaën, purity ≥ 97%) were mixed with the same mass of deionized water (ρ > 18 MΩ), stirred and placed inside of the reactor cavity. The filled reactor was dried at 100 °C for 60 min and heated up to 650 °C for 20 min with a heating rate of 10 °C min^{-1} to ensure the stability of the catalytic bed at high temperatures.

For the catalytic partial oxidation (CPO) of n-butane (Eq. 1), a higher mole amount is present at the reactor outlet according to thermodynamic calculations, leading to an increase in pressure drop. The design of the micro-reformer minimizes the effect of increased pressure drop along the reactor path by having a higher reactive volume towards the outlet of the reactor and at the same time a larger outlet cross-section. In this way, dead volumes are minimized.

$$n\text{-}C_4H_{10} + O_2 \rightarrow 4\ CO + 5H_2 \qquad \Delta H_{298\ K} = -316\ kJ\ mol^{-1} \quad (1)$$

Micro-solid oxide fuel cell membranes

Pre-etched 380 µm thick silicon substrates consisting of 30 low-stress low-pressure chemical-vapor-deposited (LP-CVD) SiN_x membranes (Embedded Microsystems Bremen GmbH) with dimension of 390 µm × 390 µm were used to fabricate the micro-SOFC membranes (Figure 1) [31, 32]. Deposition of fully crystalline columnar 3 mol% yttria-stabilized-zirconia (3YSZ) thin films on the substrate was done at 700 °C by pulsed laser deposition (PLD). The PLD target was sintered from 3YSZ powder (Tosoh Corp.) at 1400 °C for 4 h. The ablation was performed in a PLD workstation (SURFACE systems+technology GmbH & Co. KG) with a KrF Excimer Laser (26000 pulses at 10 Hz). The distance between the target and the substrate was 5.5 cm. The depositions were performed at 0.27 Pa in an oxygen atmosphere. The deposition parameters and the electrolyte composition were chosen to optimize the micro-SOFC membrane electrical properties, microstructure and thermo-mechanical stability [33-35]. After the electrolyte deposition, the underlying SiN_x layer was removed by reactive ion

etching (RIE 80, Oxford Instruments, Oxford). The etching was done in 50 sccm CHF_3 and 5 sccm O_2 gas flow at 0.01 Pa and 100 W for 200 s. Finally, Pt (purity > 99.99 at.%, Sindlhauser Materials) was deposited onto both sides of the 3YSZ by magnetron sputtering (PVD coatings). The power was set to 100 W in 10 Pa with an Ar gas flow of 10 sccm. On the top side (later the cathode side), a shadow mask was used to separate the individual electrodes, whereas the bottom side (later anode side) consisted of one electrode for all micro-SOFC membranes. The Pt-load for the active membrane area was 59 wt.%, this is calculated on the basis of non-degraded electrode thickness of 60 ± 20 nm each. The electrodes were contacted via Pt paste (C3605 P, Heraeus Holding GmbH) and flat-pressed Pt wires (MaTecK GmbH) with a diameter of 80 µm and were fixed with cement paste (TAKETSUNA Manufactory CO., LTD) as described in reference [31].

Assembly

For the assembly, a micro-reformer was glass-sealed (Ferro IP760c, Ferro Corporation) to the heated end ("hot"-end) the functional carrier. Hermetic sealing was achieved after firing in air at 700 °C for 20 min with a weight of 80 g. The micro-SOFC chip was subsequently glued with cement paste (TAKETSUNA Manufactory CO., LTD) to the underlying micro-reformer (Figure 1). The dimensions of the glass carrier and of the micro-reformer are slightly different to those reported in our earlier works [5, 11, 28-30, 36]. They were adjusted to meet the dimensions of the chip containing the micro-SOFC membranes in order to avoid closing off membranes by the cement paste used for bonding.

Testing setup

Insulation

For the gas composition as well as the electrochemical analysis, the assembled device was insulated up to the gas inlet and outlet with two WDS-Ultra blocks (Porextherm Dämmstoffe

GmbH) and Fiberfrax® ceramic paper (Unifrax Corporation). Both, gas inlet and outlet at the "cold"-end of the functional carrier, were always kept below 50 °C [28]. The temperature at the "hot"-end was measured by a thermocouple touching the top of the Si-chip containing the micro-SOFC membranes.

Gas composition analysis

The CPO performance of the micro-reactor was measured by assembling a Si-chip (without micro-SOFC membranes) on top of the reformer. Catalytic partial oxidation reaction ignition was accompanied by a temperature jump caused by the exothermic reaction. The jumps were determined by two thermocouples placed on top of the Si-chip with an accuracy of ± 4 °C. The operation temperature, T_{op}, is defined as the temperature at which steady-state conditions were obtained. The effluent gas stream composition was measured by a gas chromatograph equipped with a thermal conductivity detector (6890 GC, with a HP-PlotQ column, Agilent). The molar product gas balances for C, H and O atoms were reproducible within 5 % for all experiments. The CPO performance was measured in terms of n-butane conversion, hydrogen and syngas yield as well as molar fractions of H_2O, H_2 and CO in the outlet gas stream. The syngas yield and the hydrogen yield are defined as $\psi_{syn} = 100\,(nH_2 + nCO)/9$ and $\psi_{H2} = nH_2/(5n \cdot \text{n-}C_4H_{10})$, respectively, where n is the total amount of moles of a substance.

Electrochemical characterization

The electrochemical performance of the individual SOFC membranes was measured in the temperature regime between 400 °C and 600 °C using a stoichiometric mixture for the CPO reaction (10 vol.% n-butane in air) fed to the reformer. The total inlet gas flow entering the micro-reformer was varied between 50 sccm and 250 sccm, whereas static (laboratory) air was used at the micro-SOFC cathode side. Electrochemical impedance spectroscopy and current-voltage characteristics were measured by an impedance bridge (Zahner IM6,

ZAHNER-Elektrik GmbH & Co.KG). Three individually contacted micro-SOFC membranes were measured one after the other between 500 mHz and 4 MHz using an oscillation amplitude of 20 mV at open circuit voltage in air on the cathode and anode side. The current-voltage characteristics were tested under static air on the cathode side and the *in situ* reformed n-butane from the micro-reformer at the anode side.

The exchange current density was extracted by fitting the current response at low current densities using equation (2) [37].

$$E(J) = E_0 - \boldsymbol{b} \times \ln\frac{J+\boldsymbol{j_{int}}}{\boldsymbol{j_0}} - JR - \boldsymbol{m}e^{-\boldsymbol{n}J} \quad (2)$$

In equation 2, E is the cell voltage at the current density J, E_0 is the open circuit voltage, $\boldsymbol{j_{int}}$ is the internal current density, $\boldsymbol{j_0}$ is the exchange current density, R is the ohmic resistance of the cell which was approximated by the electrolyte resistance and **b**, **m**, and **n** are fitting parameter. In the results and discussion section, we extract and discuss the exchange current density of the entire cell from equation (2). The electrolyte resistance was extrapolated using the data from the impedance measurements performed during heating in air.

Microstructure analysis

Top-view micrographs of the micro-SOFC thin films after testing were acquired by a scanning electron microscope (FEG-SEM, Zeiss LEO Gemini 1530) with an in-lens detector. Transmission electron microscopy (TEM) in bright-field mode (BF) and scanning transmission electron microscopy (STEM) in high-angle annular dark-field (HAADF) mode were used to characterize the cross-sectional microstructure of the thin films after fuel cell testing. The microscope was a FEI Tecnai F-30 (field emission gun) with an accelerating voltage of 300 kV and a post-column CCD camera. The TEM lamella was prepared by

focused ion beam (FIB) etching technique on a NVision 40 (Zeiss) with a gallium liquid metal ion source, a gas injection system and a micromanipulator (MM3A, Kleindiek). After electron beam deposition of carbon, thin films were protected by a carbon cap. The TEM lamella was cut free with trenches from both sides with 13 nA and 3 nA at 30 kV. After the lift-out was performed, the lamella was polished to ion transparency with currents down to 10 pA at 30 kV. Amorphization was diminished by low kV showering for several seconds at 5 kV and 2 kV.

Results and Discussion

In Figure 1a, images of the prefabricated components, i.e. micro-SOFC, micro-reformer and functional carrier are shown on the left side. On the right side, a scheme of the assembly with the used materials is sketched. A photograph of the device prior to testing is shown in Figure 1b. Here the gas inlet is already connected to the device. In this testing device, the "hot"-end and "cold"-end of the functional carrier are far apart to be able to connect the gas supply line directly to the device. In a commercial device, the gas tank would be integrated in the system, which will allow a much denser packaging. Several publications exist on the feasibility of entire system and possible energy sources for the start-up energy [5, 6, 38], here we focus only on the subsystem – micro-SOFC, micro-reformer and heater gas-supply (functional carrier).

Gas composition analysis

The performance of the micro-reactor was tested in a thermally self-sustained mode as described elsewhere [30]. In order to have comparable conditions for the experiments with the

integrated SOFC-chip, the temperatures at steady state was targeted between 500 °C and 570 °C. The total inlet flow rates were similar to those investigated with the micro-SOFC chip assembly and ranged between 150 sccm and 190 sccm, which resulted in space times of the reactants in the catalytic bed between 15 ms and 21 ms. The flow rate (amount of reactants) and therefore the space time determines the measured temperature of the reactor. The start of the CPO reaction was indicated by a sudden temperature increase caused by the released exothermic energy (Eq. 1). The gas analysis results for the CPO of n-butane are given in Table 1. The exhaust gas was analyzed after 15 – 20 min of reaction at the specified flow rate. At 190 sccm, averaged values are given for four consecutive measurements. The conversion rate of n-butane increases with increasing temperature; the temperature increase has a higher impact than the increase in flow rate. The reactor generates 12 at.% to 28 at.% of hydrogen which can be used as fuel and fed on the micro-SOFC membrane anodes. Earlier studies with the same catalyst, but different geometry and flow rates showed similar hydrogen yields [10, 29, 30]. Pla *et al.* [39] reported on the design of a micro-reformer, which will convert ethanol to hydrogen, however, no performance data are published yet.

Table 1: CPO results at different flow rates. At 190 sccm, averaged values are shown for four consecutive measurements between 563 °C and 570 °C for a period of 95 min.

	150 sccm at 505 °C	170 sccm at 534 °C	190 sccm at 563 °C-570 °C
C_4H_{10} conversion, at.%	43.1	51.0	63.2 ± 1.7
H_2 yield, at.%	31.9	44.4	58.5 ± 1.8
Syngas yield, at.%	30.6	40.5	54.9 ± 1.7
x H_2, - [1)]	12.2	19.2	28.4 ± 0.9
x CO, - [1)]	8.9	12.4	19.6 ± 0.7
x H_2O, - [1)]	5.7	4.7	4.4 ± 0.4

[1)] Molar fraction.

Thermal analysis

The device was heated up to 410 °C by the integrated heaters of the glass carrier. During this start-up heating, a 50 sccm air flow on the anode side and static (laboratory) air on the cathode side of the SOFC membranes was used. During this heating step in air, impedance spectra of the symmetrical membranes were recorded. The Nyquist plot consisted of two arcs: an electrolyte arc at high frequencies and an electrode arc at low frequencies. The electrolyte conductivity was calculated to be 6.9×10^{-5} S cm^{-1} at 245 °C and 1.9×10^{-3} S cm^{-1} at 330 °C which is in good agreement with literature data [35]. The 3YSZ conductivity also confirms that the temperature measurement on top of the Si-chip reflects the temperature of the membranes. At 410 °C, 10 vol.% of n-butane was added to the air flow. By gradually increasing the total gas flow at the anode side and decreasing the voltage applied to the heater, a self-sustained reaction was achieved at 470 °C. Afterwards, the heating of the device was solely sustained by the exothermic partial oxidation of n-butane within the micro-reformer and was independent of the external power supply, which was thus switched off. The temperature was increased further by increasing the total flow rate to the reactor and therefore the anode side. Thus the operation temperature of the micro-SOFC membranes could be adjusted and controlled. Shao *et al.* [27] achieved in a very different set-up, namely a macroscopic, single chamber solid oxide fuel cell with a thickness of about 0.8 mm and reformed propane over catalytically active 10 µm thick Ru-ceria layer, a similar thermally self-sustained state with an internal indirect reformation; however, the start-up was done in a furnace and not like in this work with an integrated heater.

Electrochemical analysis

In Figure 2a, representative current-voltage characteristics of one representative micro-SOFC membrane are shown for two temperatures. An open-circuit-voltage (OCV) of 1.0 V was achieved up to a temperature of 565 °C, which indicated that the sealing of the device and the 300 nm thick PLD 3YSZ membranes are gastight. For the generated gas mixture at 550º C, a theoretical OCV of 1.07 V was calculated. This value is in good agreement with the measured values (see supplementary material) and is based on the individual OCVs of the electrochemically-active gas molecules H_2, CO, CH_4 and C_4H_{10} and their possible reactions. The second is also confirmed by the STEM analysis (Figure 3c). At higher temperatures, the cement paste starts to leak which results in a lower OCV of 0.6 V (not shown). A drastic temperature increase up to 600 °C within seconds, due to further oxidation of the fuel by the incoming air through the leakages, was then observed. All micro-SOFC membranes survived the testing procedure. This demonstrates that the free-standing 3YSZ membranes have excellent thermomechanical stability under compressive stress [32, 34]. The cathode was severely agglomerated after this high temperature as shown in Figure 3. The platinum cathode consists of isolated islands whereas the anode is still a ~ 40 nm thin film and exhibits only the very first stage of coarsening. This is in contrast to findings of Kerman *et al.* [20] who reported faster diffusion and therefore agglomeration of platinum in hydrogen atmosphere. A similar behavior of a Pt cathode was found by Schlupp *et al.* [40] on free-standing aerosol-assisted CVD YSZ membranes. Their YSZ has a very similar microstructure to the PLD 3YSZ used in this study. The swifter agglomeration of the platinum cathode is ascribed to the roughness of the electrolyte whose top-side exhibits tip-shape due to the columnar growth. Below about 0.7 V, the current-voltage (I-V) curves are reproducibly unstable, even though the temperature as well as the flow rates did not change. The I-V curves were measured in the

potentiostatic mode only. Hanke-Rauschenbach *et al.* [41] call such behavior a N-shaped negative differential resistance (N-NDR) type current-voltage curve. It is highly improbable that fuel depletion caused this behavior as more than 10 vol.% of hydrogen was generated at the reformer [42]. The high hydrogen content makes it unlikely for a competing reaction with slower kinetics, like the oxidation of CO or n-butane, to occur at the anode [42]. Blocking catalytically-active sites by another molecule with stronger adsorption to the Pt cannot be ruled out [41]. A similar behavior was observed and modeled for polymer electrolyte fuel cells and was related to condensed water of the system [43]. Even though our device runs at higher temperatures, the gas outlet is at room temperature, which could have resulted in condensation of the water in the gas outlet generated by the CPO as well as by the electrochemical reaction at the micro-SOFC anode; however, no condensed water was observed in the gas outlet after testing. Exchange current densities were calculated according to equation (2) [37] for the entire cell for the low-current region (< 0.7 V) of the current-voltage curves. An exemplary fit is shown in Figure 2a, while the exchange current density plot as a function of temperature is shown in Figure 2b. All fitting results are included in the supplementary material. The exchange current density of the entire cell shows a thermally activated behavior with an activation energy of 4.8 eV. The fitting value at 595 °C is not included here due to its very low OCV (discussed above). The exchange current densities are compared to the data of flat and corrugated micro-SOFC membranes measured in hydrogen fitted with the Tafel equation [11]. At temperatures of around 450 °C, the exchange current densities are similar, even though the total power density measured by Chao, Hsu, Cui and Prinz [11] is higher. At higher temperatures, the exchange current density of the entire cells measured here is almost one order of magnitude higher than the exchange current density of the nanostructured SOFC cells in reference [11]. The higher exchange current density but lower power density measured here are most likely due to the voltage instability found in the I-V-curves of the system. The high exchange current density of our membranes is a promising

result for the microstructure of electrodes before agglomeration. A maximum power density of 23 mW cm^{-2} and 47 mW cm^{-2} at 500 °C and 565 °C were achieved, respectively (Figure 2a). This performance is rather low when compared to best micro-SOFC membranes performance of 1.3 W cm^{-2} at 500 °C [11]. Micro-SOFC operated with humidified natural gas reformed directly at the anode showed power density of 800 mW cm^{-2} at 530 °C [22]; however, this data was measured with an external heating source whereas the here reported power densities are achieved with self-sustained heating and on-chip reformed hydrogen which is directly fed to the micro-SOFC membranes. Considerably higher power densities are expected in case more stable electrodes are used that do not show agglomeration as well as the instability is prevented [20, 44, 45]. Also, different electrode materials than pure Pt are promising, whereby most of them are based on metals [12, 21, 25, 45, 46] and metal-ceramic composites [17, 25, 27, 47-49]. Pure ceramic electrodes [25, 50-55] show also encouraging results. The total power density of the systems 'hot'-end is around 2 mW cm^{-3}, this is calculated on the rather conservative basis of one chip with 30 membranes and a total volume of 1 cm^3. Additional micro-SOFC chips would increase the total power density drastically (2 mW per chip), but would only increase the total volume by a forth per chip. The high gas flow rate of more than 150 sccm results in poor gas utilization as well as low electrical efficiency. The high gas flow rates were used to ensure that the performance of the device is not limited by the gas supply at the micro-SOFC membrane. The performance of the reformer was tested at gas flow rates as low as 30 sccm and it showed excellent performance [30]. The scope of this manuscript was to test and characterize the integrated system with micro-SOFC, micro-reformer and functional carrier. In future the components will be optimized for a high power generation.

Conclusions

The assembly and operation of an integrated system of micro-SOFC membranes, a micro-reactor and a functional carrier is successfully demonstrated in this paper. The system is operated using n-butane in air, which are internally partially oxidized by the Rh-nanoparticle based catalytic bed in the micro-reformer. In the reformer this exothermic reaction is successfully ignited at 410 °C by an integrated heater. At temperatures higher than 470 °C the system is self-sustained. With the internal reformation, a H_2 yield of up to 60 at.% is achieved. The operation temperature is tuned by adjusting the n-butane/air flow to the reformer. An open circuit voltage of 1.0 V was measured at the micro-SOFC membranes. A maximum power density of 47 mW cm^{-2} and an exchange current density of 50 mA cm^{-2} at 565 °C for an individual membrane are achieved. All 30 micro-SOFC membranes are still intact after testing; however, the electrodes degraded.

Acknowledgements

The authors thank Dr. Ji-Won Son from the Korean Institute of Science and Technology for fruitful discussions. The authors acknowledge the technical support by the FIRST cleanroom team and Electron Microscopy Center of ETH Zurich (EMEZ). B.S. and H.G. acknowledge the financial support of the “Size matters”-project, Switzerland. The financial support from the Swiss National Science Foundation (SNSF, Project No. CRSI22-126830 and grant 200021_143424) is gratefully acknowledged. L.J.G. gratefully acknowledges the support of the MEXT center of Kyushu University, Fukuoka, Japan.

Contributions

B.S., A.E., A.S. and B.J. fabricated, tested and analyzed the device with the technical help of M.N., M.P., A.B., T.M. and C.M.. R.T. and P.H. helped fabricating the device. J.M. performed the TEM analysis. H.G. helped with the data analysis. B.S. wrote the manuscript with the help of A.E., A.S. and B.J.. A.B., H.G., M.P. and L.G. critically revised the manuscript. All authors discussed the results and their interpretation.

References

[1] in: http://www.horizonfuelcell.com, 15.01.2014.
[2] in: http://www.beupp.com, Horizon, 15.01.2014.
[3] in: http://www.mtimicrofuelcells.com, 15.01.2014.
[4] C. Meier, T. Hocker, A. Bieberle-Hütter, L.J. Gauckler, Int. J. Hydrogen Energy, 37 (2012) 10318-10327.
[5] A. Bieberle-Hütter, D. Beckel, A. Infortuna, U.P. Muecke, J.L.M. Rupp, L.J. Gauckler, S. Rey-Mermet, P. Muralt, N.R. Bieri, N. Hotz, M.J. Stutz, D. Poulikakos, P. Heeb, P. Müller, A. Bernard, R. Gmür, T. Hocker, J. Power Sources, 177 (2008) 123-130.
[6] A. Bieberle-Hutter, A.J. Santis-Alvarez, B. Jiang, P. Heeb, T. Maeder, M. Nabavi, D. Poulikakos, P. Niedermann, A. Dommann, P. Muralt, A. Bernard, L.J. Gauckler, Lab on a Chip, 12 (2012) 4894-4902.
[7] in: http://www.nectarpower.com/, 15.01.2014.
[8] R.W. Barton, A. Franz, S.B. Schaevitz, in: W.I.P. Organization (Ed.), 2006.
[9] S.B. Schaevitz, A. Franz, Z. Byars, R.W. Barton, in, 2007.
[10] C.-W. Kwon, J.-W. Son, J.-H. Lee, H.-M. Kim, H.-W. Lee, K.-B. Kim, Adv. Funct. Mater., 21 (2011) 1154-1159.
[11] C.-C. Chao, C.-M. Hsu, Y. Cui, F.B. Prinz, ACS Nano, 5 (2011) 5692-5696.
[12] M. Tsuchiya, B.-K. Lai, S. Ramanathan, Nat Nano, 6 (2011) 282-286.
[13] I. Garbayo, A. Tarancón, J. Santiso, F. Peiró, E. Alarcón-Lladó, A. Cavallaro, I. Gràcia, C. Cané, N. Sabaté, Solid State Ionics, 181 (2010) 322-331.
[14] S. Rey-Mermet, Y. Yan, C. Sandu, G. Deng, P. Muralt, Thin Solid Films, 518 (2010) 4743-4746.
[15] A. Evans, A. Bieberle-Hütter, J.L.M. Rupp, L.J. Gauckler, J. Power Sources, 194 (2009) 119-129.
[16] H. Huang, M. Nakamura, P.C. Su, R. Fasching, Y. Saito, F.B. Prinz, J. Electrochem. Soc., 154 (2007) B20-B24.
[17] Y. Takagi, S. Adam, S. Ramanathan, J. Power Sources, 217 (2012) 543-553.
[18] K. Kerman, B.-K. Lai, S. Ramanathan, Advanced Energy Materials, 2 (2012) 656-661.
[19] Y. Takagi, B.-K. Lai, K. Kerman, S. Ramanathan, Energy & Environmental Science, 4 (2011) 3473-3478.
[20] K. Kerman, B.-K. Lai, S. Ramanathan, J. Power Sources, 196 (2011) 2608-2614.
[21] B.-K. Lai, K. Kerman, S. Ramanathan, J. Power Sources, 196 (2011) 6299-6304.
[22] Y. Takagi, K. Kerman, C. Ko, S. Ramanathan, J. Power Sources, 243 (2013) 1-9.
[23] D. Shekhawat, J.J. Spivey, D. Berry, Fuel Cells: Technologies for Fuel Processing, 1st Edition ed., Elsevier Science, 2011.
[24] S. McIntosh, R.J. Gorte, Chemical Reviews-Columbus, 104 (2004) 4845-4866.
[25] M. Cimenti, J. Hill, Energies, 2 (2009) 377-410.
[26] M. Huff, P.M. Torniainen, L.D. Schmidt, Catal. Today, 21 (1994) 113-128.
[27] Z. Shao, S.M. Haile, J. Ahn, P.D. Ronney, Z. Zhan, S.A. Barnett, Nature, 435 (2005) 795-798.
[28] B. Jiang, P. Muralt, P. Heeb, A.J. Santis-Alvarez, M. Nabavi, D. Poulikakos, P. Niedermann, T. Maeder, Sensor Actuat B-Chem, 175 (2012) 218-224.
[29] A.J. Santis-Alvarez, M. Nabavi, N. Hild, D. Poulikakos, W.J. Stark, Energy & Environmental Science, 4 (2011) 3041-3050.
[30] A.J. Santis-Alvarez, M. Nabavi, B. Jiang, T. Maeder, P. Muralt, D. Poulikakos, Chem. Eng. Sci., 84 (2012) 469-478.
[31] A. Evans, C. Benel, A.J. Darbandi, H. Hahn, J. Martynczuk, L.J. Gauckler, M. Prestat, Fuel Cells, 13 (2013) 441-444.

[32] R. Tölke, L.J. Gauckler, U. Kunz, A. Krauss, M. Prestat, Fuel Cells, 13 (2013) 695-702.
[33] S. Heiroth, R. Frison, J.L.M. Rupp, T. Lippert, E.J. Barthazy Meier, E. Müller Gubler, M. Döbeli, K. Conder, A. Wokaun, L.J. Gauckler, Solid State Ionics, 191 (2011) 12-23.
[34] A. Evans, M. Prestat, R. Tölke, M.V.F. Schlupp, L.J. Gauckler, Y. Safa, T. Hocker, J. Courbat, D. Briand, N.F. de Rooij, D. Courty, Fuel Cells, 12 (2012) 614-623.
[35] M.V.F. Schlupp, B. Scherrer, H. Ma, J.G. Grolig, J. Martynczuk, M. Prestat, L.J. Gauckler, physica status solidi (a), 209 (2012) 1414-1422.
[36] B. Jiang, P. Muralt, T. Maeder, P. Heeb, A.J.S. Alvarez, M. Nabavi, D. Poulikakos, P. Niedermann, Procedia Engineering, 25 (2011) 811-814.
[37] S.D. Fraser, V. Hacker, J. Appl. Electrochem., 38 (2008) 451-456.
[38] M.J. Stutz, R.N. Grass, S. Loher, W.J. Stark, D. Poulikakos, J. Power Sources, 182 (2008) 558-564.
[39] D. Pla, M. Salleras, I. Garbayo, A. Morata, N. Sabaté, N. Jiménez, J. Llorca, A. Tarancón, Proceedings of the 10th European SOFC Forum, (2012) B11113-B11121.
[40] M.V.F. Schlupp, A. Evans, J. Martynczuk, M. Prestat, Advanced Energy Materials, (2013) n/a-n/a.
[41] R. Hanke-Rauschenbach, M. Mangold, K. Sundmacher, in: Rev. Chem. Eng., 2011, pp. 23.
[42] W.G. Bessler, S. Gewies, C. Willich, G. Schiller, K.A. Friedrich, Fuel Cells, 10 (2010) 411-418.
[43] M. Groetsch, in: Fakultät Elektrotechnik und Informationstechnik Otto-von-Guericke-Universit¨at Magdeburg, 2010.
[44] T. Ryll, H. Galinski, L. Schlagenhauf, P. Elser, J.L.M. Rupp, A. Bieberle-Hutter, L.J. Gauckler, Adv. Funct. Mater., 21 (2011) 565-572.
[45] T. Ryll, H. Galinski, L. Schlagenhauf, F. Rechberger, S. Ying, L.J. Gauckler, F.C.F. Mornaghini, Y. Ries, R. Spolenak, M. Döbeli, Phys. Rev. B, 84 (2011) 184111.
[46] T.P. Holme, F.B. Prinz, The Journal of Physical Chemistry C, 115 (2011) 11641-11648.
[47] D. Klotz, J. Szasz, A. Weber, E. Ivers-Tiffée, ECS Transactions, 45 (2012) 241-249.
[48] J. Szász, D. Klotz, H. Störmer, D. Gerthsen, E. Ivers-Tiffée, ECS Transactions, 57 (2013) 1469-1478.
[49] G. Muller, R.-N. Vannier, A. Ringuede, C. Laberty-Robert, C. Sanchez, Journal of Materials Chemistry A, 1 (2013) 10753-10761.
[50] B.-K. Lai, K. Kerman, S. Ramanathan, J. Power Sources, 196 (2011) 1826-1832.
[51] F.S. Baumann, J. Maier, J. Fleig, Solid State Ionics, 179 (2008) 1198-1204.
[52] J. Hayd, L. Dieterle, U. Guntow, D. Gerthsen, E. Ivers-Tiffée, J. Power Sources, 196 (2011) 7263-7270.
[53] P. Plonczak, M. Søgaard, A. Bieberle-Hütter, P.V. Hendriksen, L.J. Gauckler, J. Electrochem. Soc., 159 (2012) B471-B482.
[54] H.-S. Noh, H. Lee, H.-I. Ji, H.-W. Lee, J.-H. Lee, J.-W. Son, J. Electrochem. Soc., 158 (2011) B1-B4.
[55] I. Garbayo, V. Esposito, S. Sanna, A. Morata, D. Pla, L. Fonseca, N. Sabaté, A. Tarancón, J. Power Sources, 248 (2014) 1042-1049.
[56] E.D. Wachsman, K.T. Lee, Science, 334 (2011) 935-939.

Figures

Figure 1: a) Scheme of individual components and photographs of pre-assembled main parts: micro-SOFC chip, micro-reformer and functional carrier. b) Photograph of the finished assembly. The gas inlet is already connected to the "cold"-end of the functional carrier. See references [5, 6, 38] for further details on the single components

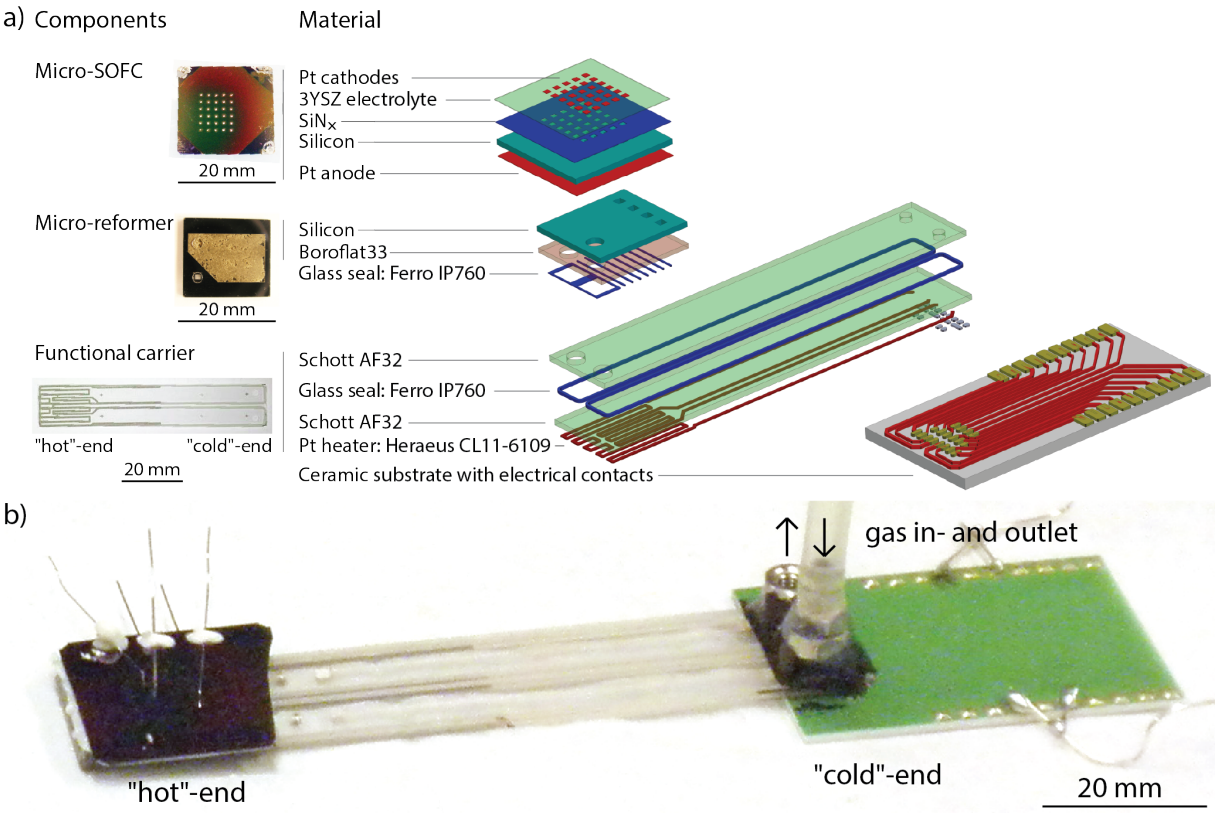

Figure 2: Typical current-voltage and performance curves (a) and all exchange current densities (b) of micro-solid oxide fuel cell membranes run on *in situ* reformed n-butane.

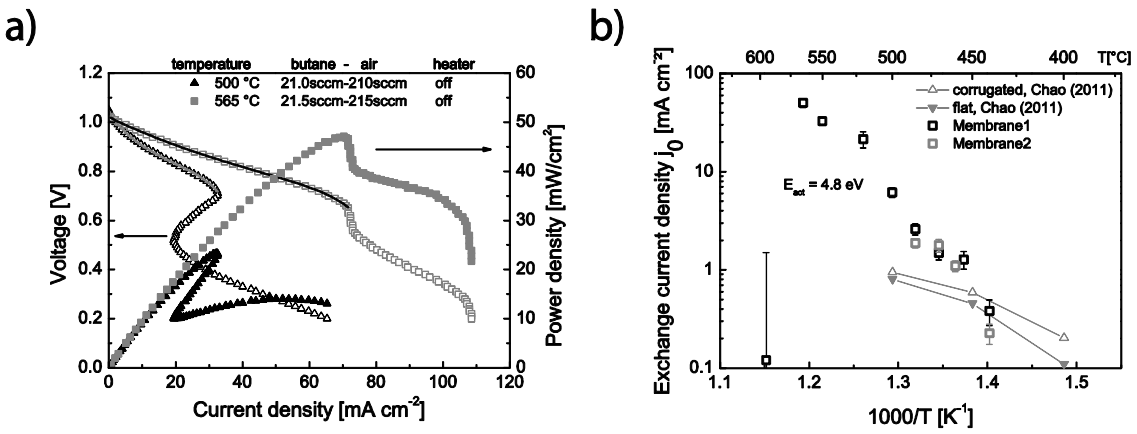

Figure 3: Microstructural characterization after fuel cell testing: a) cathode and anode top-view SEM micrographs, b) BFTEM and c) STEM cross-section view of a micro-SOFC consisting of sputtered Pt anode (35–50 nm)/PLD 3YSZ electrolyte (300 nm)/sputtered Pt cathode (100-200 nm). The hair-like structure visible on the cathode Pt islands in the TEM image comes from the ceramic paper used for insulation during testing.

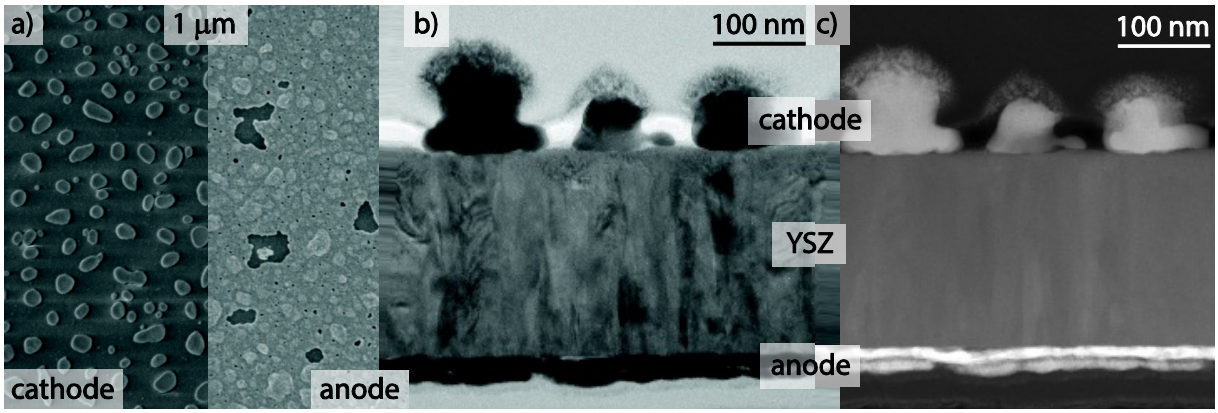

Figure captions

Figure 1: a) Scheme of individual components and photographs of pre-assembled main parts: micro-SOFC chip, micro-reformer and functional carrier. b) Photograph of the finished assembly. The gas inlet is already connected to the "cold"-end of the functional carrier. See references [5, 6, 38] for further details on the single components

Figure 2: Typical current-voltage and performance curves (a) and all exchange current densities (b) of micro-solid oxide fuel cell membranes run on *in situ* reformed n-butane.

Figure 3: Microstructural characterization after fuel cell testing: a) cathode and anode top-view SEM micrographs, b) BFTEM and c) STEM cross-section view of a micro-SOFC consisting of sputtered Pt anode (35–50 nm)/PLD 3YSZ electrolyte (300 nm)/sputtered Pt cathode (100-200 nm). The hair-like structure visible on the cathode Pt islands in the TEM image comes from the ceramic paper used for insulation during testing.

Supplementary information

The exchange current density fitting results

The exchange current density was extracted by fitting the current response at low current densities using the equation below which includes the open circuit voltage, the charge transfer overvoltage, the ohmic resistance and mass and a species transport limitation term [37].

$$E(J) = E_0 - \boldsymbol{b} \times \ln\frac{J+\boldsymbol{j_{int}}}{\boldsymbol{j_0}} - JR - \boldsymbol{m}e^{-\boldsymbol{n}J} \quad (2)$$

Where E is the cell voltage at the current density J, E_0 is the open circuit voltage, $\boldsymbol{j_{int}}$ is the internal current density, $\boldsymbol{j_0}$ is the exchange current density, R is the ohmic resistance of the cell which was approximated by the electrolyte resistance and **b**, **m**, and **n** are fitting parameter.

Table 1: Fitting results for all measured current-voltage curves of the two membranes.

Cell	T_{op}	E_0	b	j_0	j_{int}	m	n
	°C	V	V	mA cm^{-2}	mA cm^{-2}	V	cm^2 mA^{-1}
Membrane1	440	1.04	0.07 ± 0.01	0.4 ± 0.1	0.9 ± 0.2	4E-03 ± 2E-03	0.21 ± 0.03
Membrane1	455	1.05	0.14 ± 0.01	1.3 ± 0.3	2.0 ± 0.3	4E-04 ± 2E-04	0.51 ± 0.05
Membrane1	470	1.05	0.13 ± 0.01	1.5 ± 0.2	2.1 ± 0.3	3E-04 ± 3E-04	0.32 ± 0.04
Membrane1	485	1.04	0.17 ± 0.01	2.6 ± 0.3	2.9 ± 0.4	1E-04 ± 7E-05	0.59 ± 0.05
Membrane1	500	1.05	0.15 ± 0.01	6.1 ± 0.7	6.5 ± 0.7	1E-04 ± 1E-04	0.19 ± 0.02
Membrane1	520	1.05	0.30 ± 0.04	21.5 ± 3.9	22.2 ± 4.0	4E-07 ± 8E-07	0.41 ± 0.06
Membrane1	550	1.05	0.27 ± 0.02	32.9 ± 3.1	35.5 ± 3.3	7E-09 ± 2E-08	0.24 ± 0.03
Membrane1	565	1.05	0.36 ± 0.03	50.1 ± 5.0	54.3 ± 5.2	7E-06 ± 6E-06	0.13 ± 0.01
Membrane1	595	0.69	0.16 ± 1.87	0.1 ± 1.4	0.1 ± 1.4	3E-03 ± 4E-02	30.98 ± 90.25
Membrane2	440	1.05	0.05 ± 0.01	0.2 ± 0.1	0.7 ± 0.1	1E-02 ± 4E-03	0.16 ± 0.02
Membrane2	460	1.05	0.09 ± 0.01	1.1 ± 0.1	1.6 ± 0.2	3E-03 ± 2E-03	0.18 ± 0.02
Membrane2	470	1.04	0.14 ± 0.01	1.8 ± 0.3	2.1 ± 0.3	2E-04 ± 1E-04	0.57 ± 0.05
Membrane2	485	1.05	0.09 ± 0.01	1.9 ± 0.2	1.9 ± 0.2	1E-03 ± 6E-04	0.24 ± 0.03

Theoretical open circuit voltage (OCV)

In the Figure S1, the theoretical OCV for the electrochemical oxidation of hydrogen, carbon monoxide, methane, and butane between 100 and 900 °C is shown. The OCV was calculated using thermodynamic tables in reference [56] and the following equations:

$$\eta(T) = \frac{\Delta G(T)}{\Delta H} \tag{3}$$

$$\Delta G = \Delta H_{out} - \Delta H_{in} - T(\Delta S_{out} - \Delta S_{in}) \tag{4}$$

$$OCV(T) = E(T) = -\frac{\Delta G(T)}{nF} \tag{5}$$

Where $\eta(T)$ is the thermodynamic efficiency, $\Delta G(T)$ is the Gibbs free energy and $E(T)$ is the theoretical potential at temperature T, ΔH_{in} and ΔH_{out} is the input and output enthalpy, ΔS_{in} and ΔS_{out} is the input and output entropy, n is the number of electrons transferred and F is the Faraday constant.

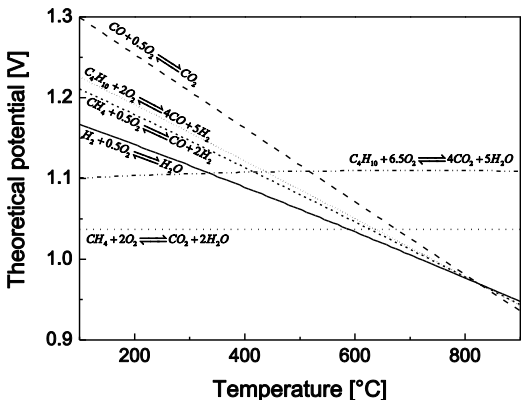

Figure S1: The individual theoretical potential of the electrochemically active gas species found in the gas mixture after the reformer.

The theoretical OCV of the gas mixture at 550 ºC is 1.07 V, which was calculated with the mol% of the individual gases. The difference between the measured OCV and the theoretical OCV can be explained by the different electrochemical oxidative reactions and the presence of inert gases like H_2O, CO_2 and N_2 on the anode side.